# Dealloying-driven local corrosion by intermetallic constituent particles and dispersoids in aerospace aluminium alloys

Kosari, A.; Tichelaar, F.; Visser, P.; Zandbergen, H.; Terryn, H.; Mol, J. M.C.

**DOI**
10.1016/j.corsci.2020.108947

**Publication date**
2020

**Document Version**
Final published version

**Published in**
Corrosion Science

Corrosion Science 177 (2020) 108947

Contents lists available at ScienceDirect

Corrosion Science

journal homepage: www.elsevier.com/locate/corsci

# Dealloying-driven local corrosion by intermetallic constituent particles and dispersoids in aerospace aluminium alloys

A. Kosari[a,*], F. Tichelaar[b], P. Visser[c], H. Zandbergen[b], H. Terryn[d], J.M.C. Mol[a]

[a] Department of Materials Science and Engineering, Delft University of Technology, Mekelweg 2, 2628 CD Delft, the Netherlands
[b] Kavli Institute of Nanoscience, Delft University of Technology, Lorentzweg 1, 2628 CJ Delft, the Netherlands
[c] AkzoNobel, Rijksstraatweg 31, 2171 AJ, Sassenheim, the Netherlands
[d] Department of Materials and Chemistry, Research Group Electrochemical and Surface Engineering (SURF), Vrije Universiteit Brussel, Pleinlaan 2, 1050 Brussels, Belgium

ARTICLE INFO

*Keywords:*
Aerospace aluminium alloys
Quasi in-situ TEM
Cross-sectional ex-situ TEM
FIB/SEM analysis
Dealloying
Pitting corrosion

ABSTRACT

Nanoscopic characterization of heterogeneous intermetallic particles (IMPs) which microstructurally and compositionally evolve during local corrosion is crucial in unravelling the mechanisms and sequence of initial and local corrosion events. Herein, we study site-specific initiation events focused on microscopic constituent intermetallic compounds and nanoscopic dispersoids in AA2024-T3 at the nanoscale using a combined quasi in-situ and ex-situ analytical TEM approach. Our findings show a dealloying-driven local corrosion initiation at the studied IMPs that have been considered as cathodic phases traditionally. Besides, local degradation which is a result of galvanic interactions between dealloyed regions of IMPs and their adjacent alloy matrix is largely governed by the intrinsic electrochemical instability of intermetallic compounds.

## 1. Introduction

Microstructurally complex aluminium alloys (AAs) constitute a structural material class with an essential high-strength-to-weight ratio, desirable for aerospace applications [1]. However, aerospace AAs are undesirably prone to different types of electrochemical degradation as a direct consequence of microstructural heterogeneities [2–10]. Given the pivotal importance of engineering safety in aerospace structures, detailed understanding must be acquired to describe microstructurally detrimental corrosion descriptors in deterministic terms where the literature still lacks a comprehensive mechanism [11].

Corrosion in aerospace AAs is inherently site-specific, commonly initiating in the form of localized attack at individual IMP locations [9,12–15] where the surrounding alloy surface is covered by a protective aluminium (hydr)oxide passive layer [16,17]. Intermetallic compounds are in fact precipitates, constituent phases and dispersoids with diverse chemical composition in a wide range of dimensions from the nano- to microscale. Precipitates like $Al_2CuMg$ and $Al_2Cu$ emerge in response to age hardening processes and greatly contribute to the mechanical strength enhancement in aerospace AAs [18,19]. Comparatively, constituent phases are formed during solidification at high temperatures and normally not affected by subsequent heat treatments, having a minor contribution to mechanical properties [20,21]. In addition, they are relatively large ($> 1$ μm), irregularly-shaped and rather diverse in chemical composition, containing different amounts of Al, Cu, Fe, Mn and Si and characteristically crystallizing in a variety of atomic structures [22]. Dispersoids like $Al_{20}Mn_3Cu_2$ are formed purposefully in the melt for grain refinement, commonly having a submicron size and being nodular-shaped [23].

For many years, electrochemical and physicochemical studies of intermetallic compounds have brought the researchers to the conclusion that local corrosion in AAs is mainly a consequence of microgalvanic interactions of IMPs with one another or mainly with the alloy matrix in their vicinity [24,25]. Given that electrochemical reactivity is linked to chemical composition [26–29], IMPs acquire different corrosion potential than the alloy matrix when exposed to aqueous solutions [30–33]. Constituent IMPs (i.e. $Al_7Cu_2Fe$, $Al_{20}Mn_3Cu_2$ and $Al_{76}Cu_6Fe_7Mn_5Si_6$) are generally reported as potential cathodic phases that support cathodic reactions like oxygen reduction reaction (ORR) upon exposure, owing to a higher corrosion potential (Volta potential) than that of the alloy matrix [5,34–36]. This process will establish a locally basic solution chemistry in which the aluminium (hydr)oxide passive layer is undermined gradually. Such electrolyte conditions can give rise to local dissolution of the surrounding matrix commonly in the form of a circumferential trench around the IMP. This form of local dissolution, known as trenching, is reportedly governed by the intrinsic cathodic activity of the cathodic compounds [9,37]. This is in contrast to the process for anodic particles that endure self-corrosion and would

* Corresponding author.
*E-mail address:* a.kosari@tudelft.nl (A. Kosari).

https://doi.org/10.1016/j.corsci.2020.108947
Received 6 July 2020; Received in revised form 6 August 2020; Accepted 13 August 2020
Available online 19 August 2020

be pitting locations themselves, as the surrounding matrix drives anodic dissolution of the phases of relevance (i.e. $MgZn_2$ [38] and $Mg_2Si$ [39,40]).

However, recent studies with experimental techniques granting a high spatial resolution have provided new insights into incongruent behaviour of cathodic phases and seemingly similar to anodic phases, they show to undergo self-corrosion at very early stages of the exposure to aqueous environments. For instance, Zhang et al. [41] and Wang et al. [42], who used ex-situ transmission electron microscopy (TEM) to study corrosion of Al-Cu-Mg alloys, have reported the preferential dissolution of Al and Mn from $Al_{20}Cu_2Mn_3$ particles at very early stages of exposure, triggered by structural planar defects like twin boundaries. $Al_2Cu$ particles have also been reported to show a tendency for selective aluminium dissolution (dealloying) and found partially dealloyed when embedded in the alloy matrix [43]. Recently Frankel and co-workers [44] were able to probe the early stages of IMPs-induced local corrosion, using a combined scanning electron microscopy/scanning Kelvin probe force microscopy (SEM/SKPFM) approach. In line with their prior works [45,46], they indicated that preferential dissolution of the active element aluminium in $Al_7Cu_2Fe$(Mn) takes place at a faster rate than the matrix dissolution. Such observations challenge the traditional microgalvanic coupling concept based on difference in corrosion potential [32] (or Volta potential [47]) of IMPs with respect to the alloy matrix. However, in spite of the recent findings, the literature still lacks a thorough mechanistic description of how local corrosion initiates and propagates around dispersoids and constituent phases at different stages of degradation. Thus, time-resolved nanoscopic information which is crucial for reliable and accurate corrosion modelling and simulations to predict the service lifetime of AA structures are yet to be achieved [36,48].

In this work, we continue the endeavour towards deterministic characterization of time-resolved local corrosion focused on macroscopic constituent intermetallic compounds and nanoscopic dispersoids conventionally categorized as cathodic phases in aerospace AA2024-T3. A challenge in this regard is to provide nanoscopic observations and analysis of microstructurally and compositionally evolutions during different stages of local corrosion at the same location. To this aim, quasi in-situ TEM is a potentially powerful approach and has been widely used in recent studies of corrosion [40,49–52]. As a drawback, quasi in-situ TEM has to be conducted on electron-transparent thin specimens which can merely represent very initial stages of corrosion [53]. Therefore, in this study we combine it with cross-sectional ex-situ TEM experiments and also supplementary focused ion beam/scanning electron microscopy (FIB/SEM) morphological investigations to explore local degradation phenomena in AAs from surface initiation to in-depth propagation.

## 2. Material and Methods

### 2.1. Top-view quasi in-situ TEM

This part of the experiments was carried out by intermittently observing an identical location on argon ion-milled thin specimens exposed to 0.01 M NaCl solution outside the electron microscope. After each exposure event, the specimens were rinsed off with distilled water for a few seconds. Then, water on the specimens was immediately absorbed by delicate-task wipes and dried under a lamp. The specimens were subjected to plasma-cleaning for 5 min right before re-inserting into the TEM column. A Tecnai F20ST/STEM 200 keV was employed to perform typical high-angle annular dark field/scanning TEM (HAADF/STEM) imaging, energy dispersive spectroscopy (EDS) elemental mapping and also high resolution TEM imaging. Note that HAADF-STEM images are highly sensitive to variations in the effective atomic numbers (Z-contrast and local thickness) in the studied regions [54]. For energy dispersive spectroscopy (EDS) elemental mapping, an Oxford Instruments X-Max$^N$ 100TLE windowless detector was used.

### 2.2. Cross-sectional ex-situ TEM

AA2024-T3 sheets were hand-ground down to 1200 emery paper in water, followed by polishing using 0.5 and 0.05 µm alumina slurry in a non-aqueous solution on a soft cloth. The samples were immersed in quiescent 0.01 M NaCl solution for different exposure times, followed by rinsing with distilled water. Subsequently, the surface corrosion-attack morphology of the samples was examined with SEM. Afterward, thin cross-sections of specific corroded particles were fabricated with a Thermo Fisher Helios G4 FIB and positioned on copper half grids for later TEM examinations using a dedicated lift-out procedure [55]. To protect the corroded surfaces while gallium ion-milling, a 200-nm-thick layer of carbon was deposited initially with a 2-keV electron beam, followed by ion-beam deposition until reaching a carbon thickness of approx. 1 µm. Although quasi in-situ top-view observations are highly useful to probe the early stage initiation events, the cross-sectional investigations reveal the local corrosion propagation deeper into the sample.

### 2.3. FIB/SEM investigations

FIB/SEM serial cross-sectioning was performed on corroded IMPs in a polished sample exposed to 0.01 M NaCl for 19 h. The top-view and cross-sectional SEM morphological studies were carried out at 5 keV collecting emitted secondary electrons (SE) in ultra-high-resolution mode. FIB sectioning was conducted in a blind-mode; the ion beam was used merely for cross-sectional milling. This allows us to skip doing Pt or C deposition for protection of the top surface from ion-beam damage.

## 3. Results and Discussion

### 3.1. Isolated constituent $Al_{76}Cu_6Fe_7Mn_5Si_6$

Fig. 1a shows a time-resolved morphological evolution of local corrosion induced by an $Al_{76}Cu_6Fe_7Mn_5Si_6$ particle; this is the approximate composition determined with STEM/EDS. After 30 min, HAADF-STEM shows no apparent corrosion attack neither to the particle nor to the surrounding matrix. However, the magnified view of the rectangular region (Region I), shown in Fig. 1b, reveals some contrast variations indicating that nanoscopic local breakdown has taken place. As can be seen, numerous nano-sized pits which are darker in appearance due to material removal are formed over the particle, demonstrating corrosion initiation in the form of nano-pitting. We also observe pitted zones over the alloy matrix merely closest to the corroded regions of the particle, indicated by the white arrows. With prolonged exposure to 0.01 M NaCl (t = 60 min), the contrast variations simultaneously spread over the particle mostly (bordered by the red dashed line) but also over the matrix. After 120 min of exposure, corrosion has clearly attacked the top right corner of the particle and its adjacent matrix which is covered with bright cloud-like corrosion products verified as aluminium (hydr)oxide (see Fig. S1 in Supplementary data). Besides, the HAADF-STEM image taken at 150 min reveals the appearance of some bright regions on different parts of the particle, indicated by the red arrows. The EDS analysis indicates these to be copper nanoclusters termed as copper residual. At this stage, a part of the surrounding matrix showed up in the darkest contrast due to partial dissolution (Region II). As shown in the magnified STEM/EDS image (Fig. 1c), the particle and its closest matrix have undergone local corrosion. Given the EDS results, selective dissolution of aluminium, manganese and to a minor extent iron and silicon from the particle is evident, coming along with copper aggregation in a globular morphology. Closest to the dealloyed zones, the alloy matrix is fully dissolved. Prolonged exposure up to 270 min causes further local degradation of both the particle and the surrounding alloy matrix. At this stage, the STEM image taken from Region III (Fig. 1d) shows partial dissolution of the matrix where copper-rich zones were formed already

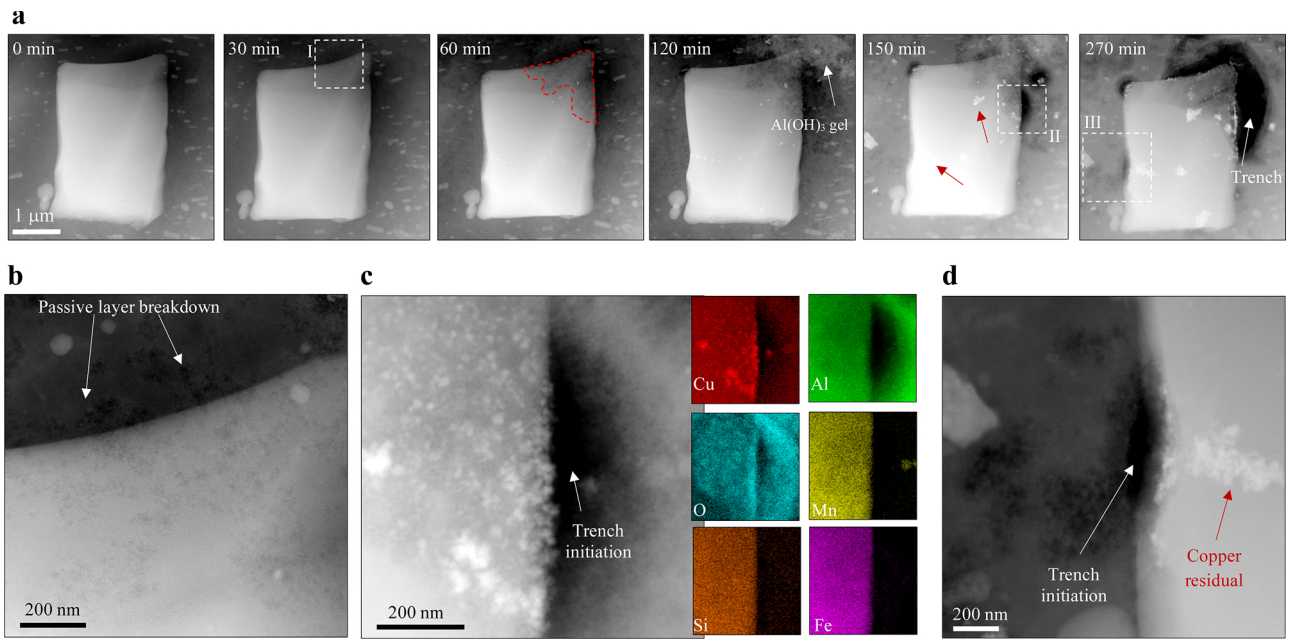


**Fig. 1.** Quasi in-situ STEM/EDS analysis of local corrosion induced by $Al_{76}Cu_6Fe_7Mn_5Si_6$ phase. (a) Time-resolved HAADF-STEM images of an $Al_{76}Cu_6Fe_7Mn_5Si_6$ particle undergoing dealloying form of local corrosion. The red arrows point to the copper residual. (b) Magnified-view HAADF-STEM image of the rectangular region (Region I) after 30 min. (c) STEM/EDS analysis of Region II at the particle/matrix interface after 150 min, revealing the aggregated region of copper due to dealloying. (d) Magnified HAADF-STEM image of Region III after 270 min. The specimen is an argon ion-milled 3-mm disk intermittently exposed to 0.01 M NaCl.

over the particle. Note that the trenching emerges merely around the dealloyed regions of the corroding particle, implying highly-local galvanic interactions.

Fig. 2a and b show top-view SEM and cross-sectional STEM/EDS analysis of two $Al_{76}Cu_6Fe_7Mn_5Si_6$ particles at the surface of polished bulk samples immersed in 0.01 M NaCl for 6 h and 19 h, respectively. The SEM image of the particle exposed for 6 h depicts a shallow trench which is a bit darker in contrast as compared to the uncorroded matrix. The particle surface is rather smooth but numerous bright spots are distinguishable on the particle itself; it is consistent with the globular morphology shown in Fig. 1c. The corresponding HAADF-STEM image taken from the particle cross-section shows a bright layer at the top of the particle; it is more pronounced in the magnified view of the rectangular region at the particle/matrix interface. As can be seen in the EDS line scan reconstructed from the indicated rectangular region in the STEM image, the top layer clearly demonstrates selective dissolution of elemental components except copper. Aluminium is the element that has dissolved severely.

Fig. 2b shows an $Al_{76}Cu_6Fe_7Mn_5Si_6$ particle exposed for 19 h. From the SEM image, the particle surface is quite rough in morphology,

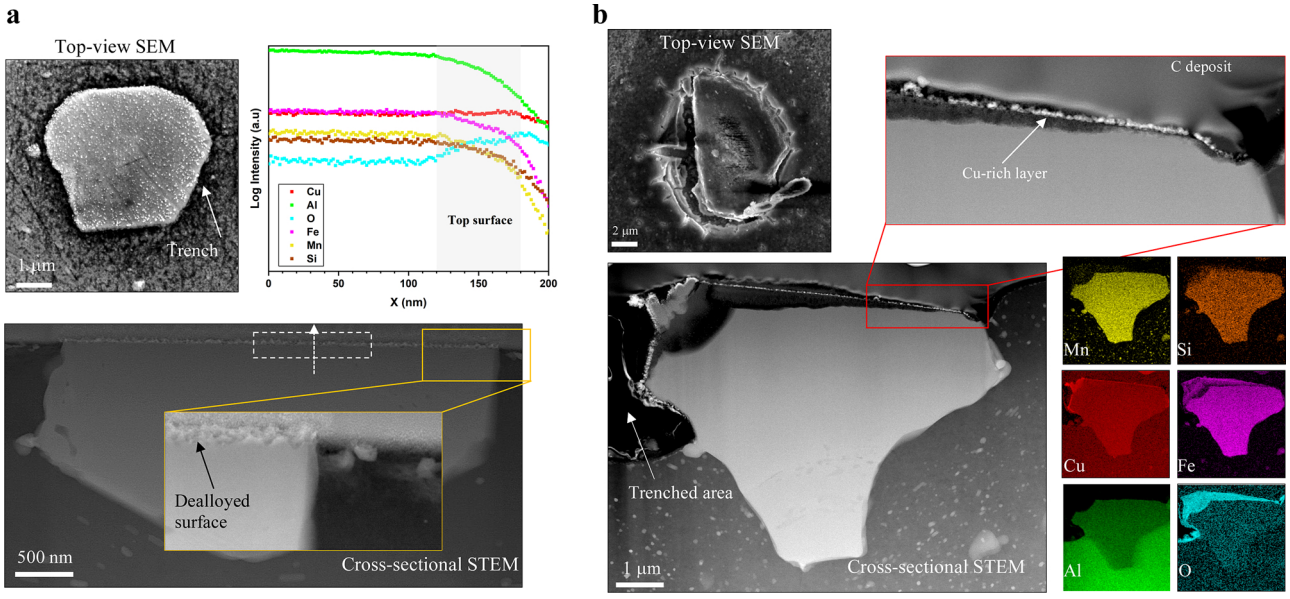


**Fig. 2.** Ex-situ SEM and TEM analysis of local corrosion induced by $Al_{76}Cu_6Fe_7Mn_5Si_6$ phase. (a) Top-view SEM and cross-sectional STEM analysis of an $Al_{76}Cu_6Fe_7Mn_5Si_6$ particle immersed in 0.01 M NaCl for 6 h. The inset is the magnified view of the orange rectangular region. The graph shows the elemental scan lines reconstructed from the rectangular region in the STEM image, revealing the top surface dealloyed. (b) Top-view SEM and cross-sectional STEM/EDS analysis of an $Al_{76}Cu_6Fe_7Mn_5Si_6$ particle immersed in 0.01 M NaCl for 19 h. The inset is the magnified view of the red rectangular region, showing the copper-rich layer on the top. The SEM images are taken using the reflected secondary electrons. The cross-sections are fabricated out of the analysed particles with FIB.

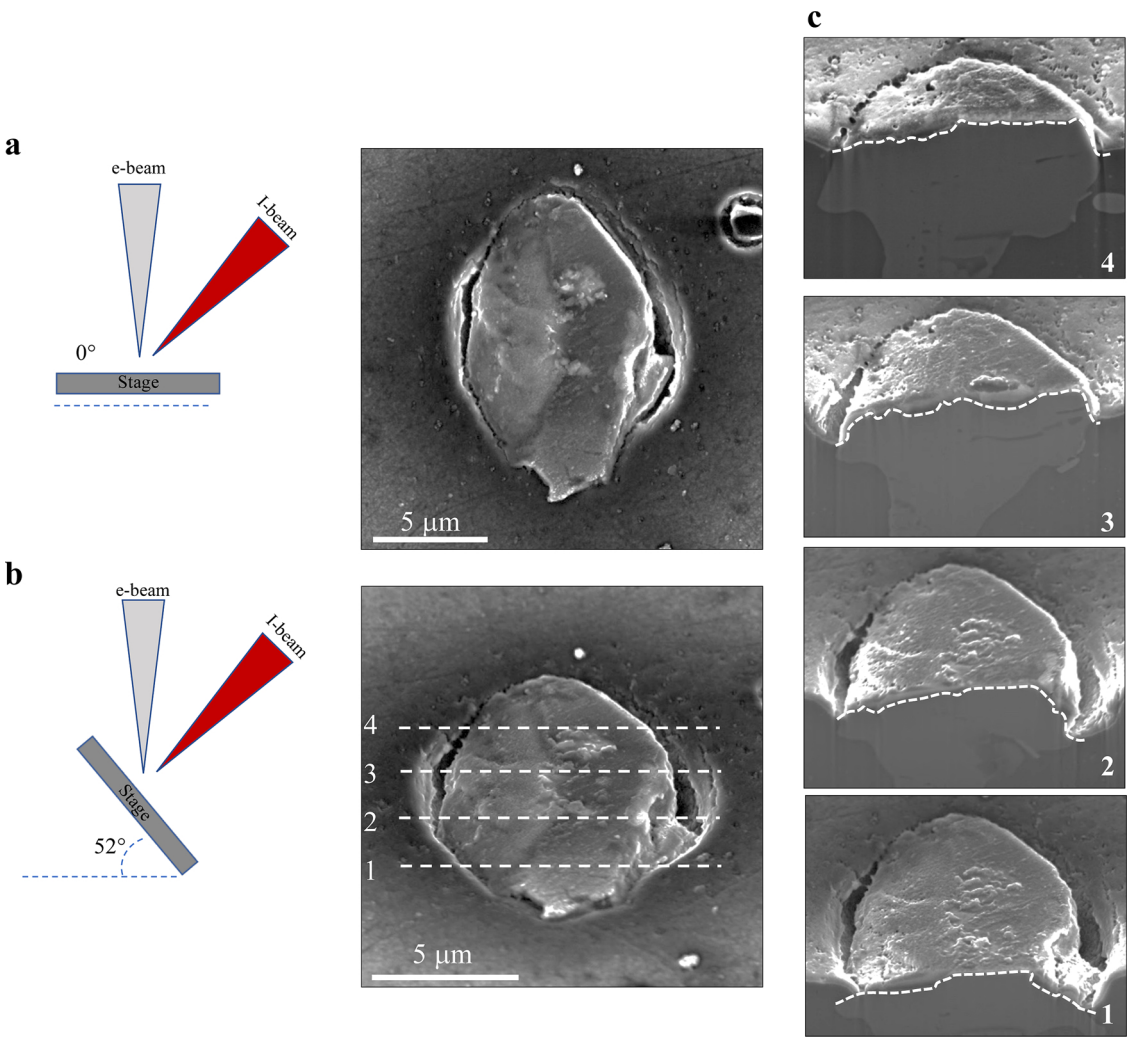


**Fig. 3.** FIB/SEM analysis of local corrosion induced by $Al_{76}Cu_6Fe_7Mn_5Si_6$ phase. (a) Top-view SEM image of an $Al_{76}Cu_6Fe_7Mn_5Si_6$ particle immersed in 0.01 M NaCl for 19 h. (b) SEM image of the same IMP when the stage is tilted at 52 °. (c) SEM images of the FIB serial sections along the lines shown in Fig. 3b. The white dashed curves separate the dealloyed region from the intact part of the particle.

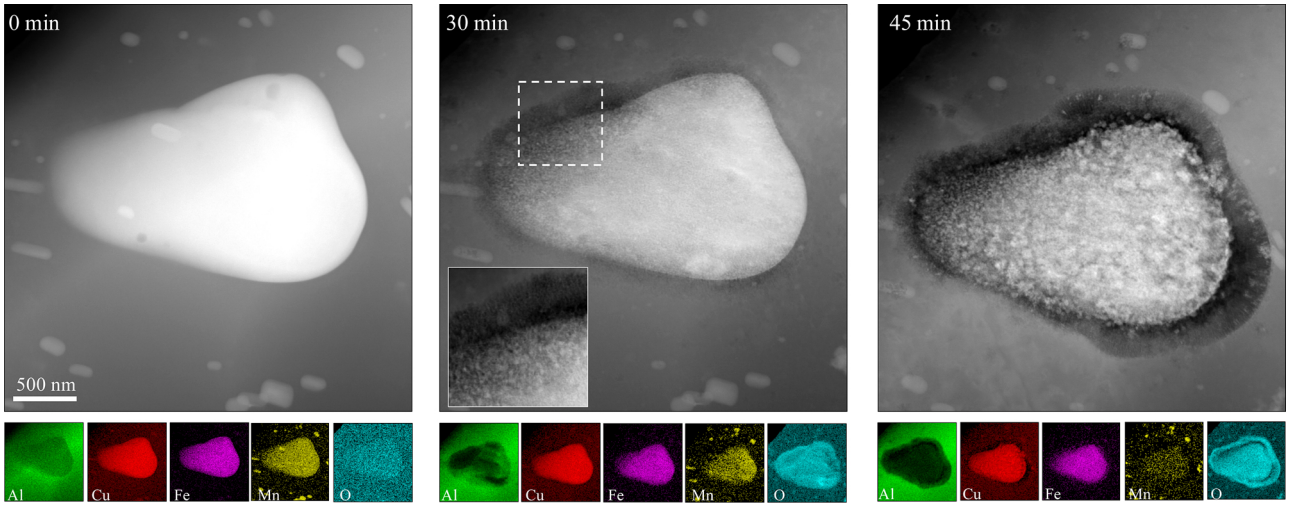


**Fig. 4.** Quasi in-situ STEM/EDS analysis of local corrosion induced by $Al_7Cu_2Fe(Mn)$ phase. HAADF-STEM images and corresponding EDS maps at different exposure times, revealing the dissolution of Al and Mn, and to a minor extent Fe from the particle. Due to Cu and Fe aggregation, the particle shows a globular morphology with time. The inset at 30 min is a closer look at the white rectangular region, revealing the dealloyed region of the particle. The specimen is an argon ion-milled 3-mm disk exposed repeatedly to 0.01 M NaCl.

compared to the particle in Fig. 2a. Moreover, corrosion has fully trenched the adjacent alloy matrix, albeit the trench has a wider opening at the left side. The cross-sectional STEM/EDS analysis shows that this particle is partially dealloyed; the corroded part is rich in copper and iron but depleted in aluminium and manganese and to a lesser extent silicon. A copper-rich layer is also seen at the upper part of the particle (see the inset corresponding to the rectangular region). Note that the matrix corrosion has propagated deeper where the particle has been more dealloyed, suggesting enhanced galvanic interactions between the copper-rich region and closely-located alloy matrix.

Fig. 3 shows the serial FIB sectioning on an $Al_{76}Cu_6Fe_7Mn_5Si_6$ particle corroded for 19 h. The top-view SEM image reveals a continuous trench around the IMP with a tight opening (Fig. 3a). Fig. 3b shows the SEM image of the same IMP when the stage is tilted at 52 °. The serial FIB sections, shown in Fig. 3c, were performed along with the white dashed lines. The cross-sectional SEM images reveal the dealloyed part of the particle brighter than the intact part, owing to huge removal of aluminium which is a light element. As can been seen, the top surface of the whole particle is dealloyed, although dealloying has penetrated deeper into some regions of the IMP (mind the white dashed curves).

### 3.2. Isolated constituent $Al_7Cu_2Fe(Mn)$

The top-view STEM/EDS results of local corrosion induced by a particle of this group are shown in Fig. 4. According to the oxygen map, we see that corrosion initially attacks the particle to a greater extent than the matrix. Comparing the EDS elemental maps before and after 30-min exposure reveals that corrosion has partially depleted the particle from aluminium and manganese, implying a dealloying form of attack. At this stage, a globular morphology is seen for the largely-dealloyed region where the alloy matrix has been partially dissolved. The inset shows the magnified view of this zone in Fig. 4. This phenomenon is in line with our observations for $Al_{76}Cu_6Fe_7Mn_5Si_6$. After 45 min, the globular morphology becomes more evident on the particle whilst the surrounding matrix has been fully trenched, as imaged with HAADF-STEM. The EDS maps have revealed that at this stage of exposure, the particle is almost depleted from aluminium. Manganese and to a minor extent iron are also dissolved while copper shows no clear change in intensity during the course of exposure. Compared to $Al_{76}Cu_6Fe_7Mn_5Si_6$, the local degradation takes place over a shorter time-scale for $Al_7Cu_2Fe(Mn)$ since it has a higher Cu content which can drive the dealloying process and galvanic interactions more effectively. More evidence can be found in Fig. S2.

Several $Al_7Cu_2Fe(Mn)$ particles on the post-corroded samples are cross-sectionally observed to get insights into how exactly this phase induces local corrosion to the surrounding alloy matrix. Fig. 5a shows the STEM image of an $Al_7Cu_2Fe(Mn)$ particle exposed for 15 min. According to the contrast variations, dealloying has penetrated deeper at the particle/matrix interface, associated with matrix trenching. The EDS line scan reconstructed from the indicated rectangular region in the STEM image clearly demonstrates selective dissolution of aluminium, manganese and to a minor extent iron. Besides, the upper part of the particle which appears as a bright layer in the HAADF-STEM image is enriched in copper and iron. Fig. 5b shows the STEM/EDS analysis of an $Al_7Cu_2Fe(Mn)$ particle at the attacked/intact interface in the sample that is immersed in 0.01 M NaCl for 6 h (Fig. S3). The estimated compositions of Region I and II reveals that the particle has undergone preferential dissolution of aluminium, manganese and even slightly iron. Dealloying has propagated into depth and left behind bright stringers. In the high-resolution EDS map, these stringers are identified as copper-rich regions that are formed by surface diffusion of copper during the dealloying process [56]. Fig. 5c shows an $Al_7Cu_2Fe(Mn)$ particle fully dealloyed and undercut from its adjacent matrix. The particle surface is quite rough in morphology (SEM image) and the corresponding cross-section reveals a coarse globular morphology. In addition, the induced local corrosion has trenched all around the particle, leading to an undercut remnant (Fig. 5c) which still contains 7.0 At% Al, 5.4 At% Fe, 42.9 At% O and Cu as balance.

Fig. 6a and b show the SEM image of a large $Al_7Cu_2Fe(Mn)$ particle when the stage is at 0 and 52 ° tilt, respectively. The sample is exposed previously to 0.01 M NaCl for 19 h. The SEM images show a deep continuous trench with a wide opening around the IMP. The serial FIB sections are presented in Fig. 6c. The FIB section along line#1 shows the particle thoroughly dealloyed where the bottom of the particle is obviously disconnected from the alloy matrix. The FIB sections along line#2 and line#3 reveal that this IMP has not been undercut yet, although the dealloyed front has penetrated quite deep into the particle. The FIB cross-section along line#4 has mainly endured dealloying and a tiny region is still intact. This indicates that the IMPs become deeper dealloyed close to the trenched area.

### 3.3. Dispersoids $Al_{20}Mn_3Cu_2$

Fig. 7a shows time-resolved HAADF-STEM images of a dispersoid undergoing local dissolution and later inducing alloy matrix trenching. The particle initially undergoes a local breakdown in the form of a nano-pit (t = 30 min). With prolonged exposure, a bright spot (verified as a copper-rich nanoparticle) appears around the pitted part of the particle (t = 60 min). After 120 min, corrosion extends over the alloy matrix closest to the locally-dissolved part of the particle. Exposed for 30 more min, a bright remnant is observed where its adjacent alloy matrix is fully dissolved in the form of a trench. To get detailed insight into compositional evolution of this phase, a specimen was exposed to distilled water for 20 min. STEM/EDS analysis of a dispersoid, shown in Fig. 7b, indicates that the particle has been dealloyed due to selective aluminium and manganese dissolution. Fig. 7c clearly shows the presence of individual nano-pits caused by dealloying over an isolated dispersoid. Although twin boundaries are reported as local dissolution sites of dispersoids [41,42], the high-resolution TEM image (inset) reveals that local dissolution has taken place for this particle in the absence of any planar defects. This phenomenon implies that $Al_{20}Mn_3Cu_2$ dispersoids like other studied phases herein have a lower electrochemical stability and readily undergo local breakdown (pitting) themselves and preferential dealloying of active elements, as compared to the alloy matrix.

### 3.4. Composite $Al_7Cu_2Fe(Mn)/Al_{76}Cu_6Fe_7Mn_5Si_6$

The study of composite IMPs is highly insightful to study the mechanisms through which different compositional domains can comparatively induce local corrosion in AAs [3]. Fig. 8a shows STEM/EDS results for a composite particle on an argon ion-milled sample after 320 min exposure to 0.01 M NaCl. The EDS analysis (i.e. Al and O map) shows that the domain with a higher copper amount, $Al_7Cu_2Fe(Mn)$, has undergone selective dissolution of aluminium. Besides, its adjacent alloy matrix is locally dissolved; this part of the alloy matrix, indicated by the white arrow, appears darker in contrast. Although the $Al_7Cu_2Fe(Mn)$ acquires a higher corrosion potential (higher galvanic driving force to trigger anodic dissolution of the alloy matrix) than the $Al_{76}Cu_6Fe_7Mn_5Si_6$, it is remarkable that aluminium has also etched away from $Al_7Cu_2Fe(Mn)$ compositional domain. This phenomenon can be better explored through cross-sectional analysis of composite particles.

In Fig. 8b, we see the SEM image (the inset) revealing a constituent particle with a discontinuously-trenched matrix, indicated by the white arrow. Our cross-sectional TEM evaluation reveals that this is in fact an $Al_7Cu_2Fe(Mn)/Al_{76}Cu_6Fe_7Mn_5Si_6$ composite particle. As denoted by the red dashed lines in the SEM image, the $Al_7Cu_2Fe(Mn)$ domain acts like a narrow ribbon separating the large $Al_{76}Cu_6Fe_7Mn_5Si_6$ part from the alloy matrix. The trench has propagated deeper around the larger $Al_7Cu_2Fe(Mn)$ domain (left side in the STEM image). Furthermore, the

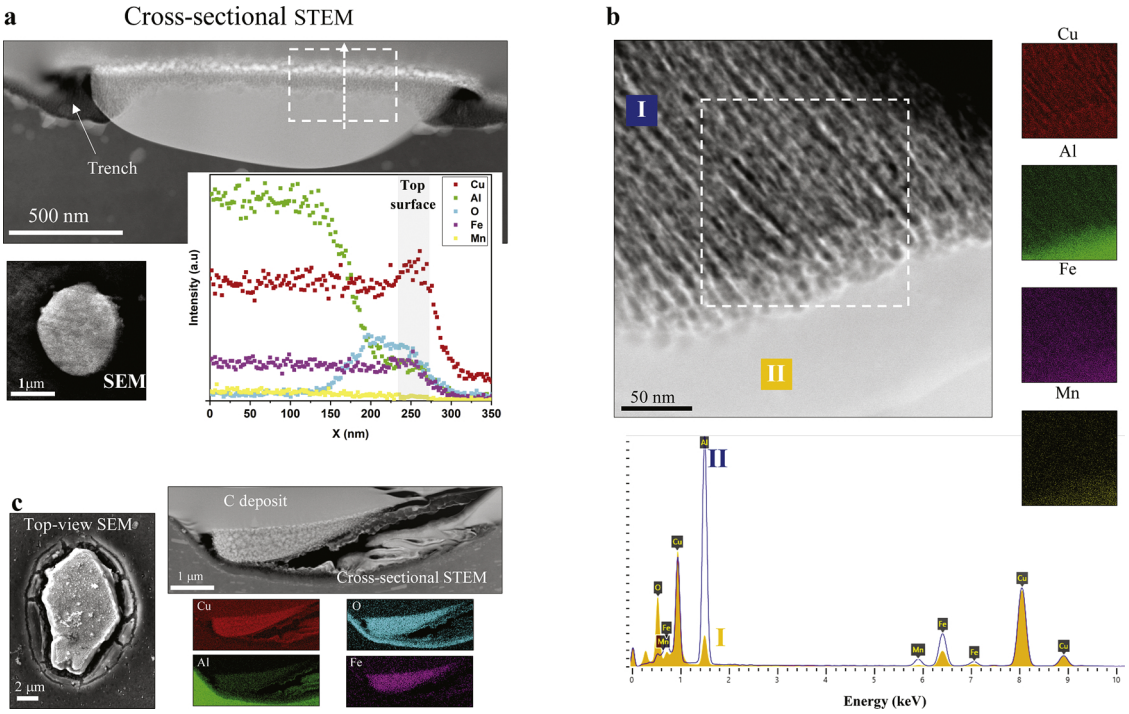


**Fig. 5.** Ex-situ analytical TEM analysis of local corrosion induced by $Al_7Cu_2Fe$(Mn) phase. (a) Top-view SEM and cross-sectional STEM image of an $Al_7Cu_2Fe$(Mn) particle immersed in 0.01 M NaCl for 15 min. The graph shows the elemental scan lines reconstructed from the rectangular region in the image, revealing preferential dissolution of aluminium and manganese and formation of a Cu-, Fe-rich layer on the top. (b) Magnified cross-sectional STEM/EDS analysis of a dealloyed $Al_7Cu_2Fe$(Mn) particle exposed to 0.01 M NaCl for 6 h. The STEM image of this particle at low magnification is shown in Fig. S3. The spectra compare the chemical composition of the corroded (I) and intact (II) regions. (c) Top-view SEM and cross-sectional STEM/EDS analysis of an undercut $Al_7Cu_2Fe$(Mn) particle immersed in 0.01 M NaCl for 6 h.

inset, the zoomed-in STEM image of the white rectangular region, shows that the $Al_7Cu_2Fe$(Mn) and $Al_{76}Cu_6Fe_7Mn_5Si_6$ are not at the same surface level. Interestingly, the dealloying attack (preferential Al and Mn dissolution) has deeply penetrated into the $Al_7Cu_2Fe$(Mn) phase but not into the $Al_{76}Cu_6Fe_7Mn_5Si_6$ domain which has just undergone surface etching. It seems that the $Al_7Cu_2Fe$(Mn) phase has a low electrochemical stability, whereby it endures faster dealloying than the $Al_{76}Cu_6Fe_7Mn_5Si_6$ domain. This phenomenon is more pronounced in Fig. 9, showing FIB/SEM analysis of a composite $Al_7Cu_2Fe$(Mn)/$Al_{76}Cu_6Fe_7Mn_5Si_6$ particle immersed in 0.01 M NaCl for 19 h. As evident, the alloy matrix adjacent to the $Al_7Cu_2Fe$(Mn) domain has been trenched widely and deeply whereas it has narrowly dissolved around the $Al_{76}Cu_6Fe_7Mn_5Si_6$ domain. The cross-sectional SEM image along the dashed line shown in Fig. 9b reveals a deep penetration of dealloying into the $Al_7Cu_2Fe$(Mn) domain. Mind the inset which is a closer look at the orange rectangular region in Fig. 9c. More evidence of the local corrosion induced by a composite particle is presented in Fig. S5.

The current observations suggest that IMPs undergo dealloying as a consequence of their electrochemical instability. However, the kinetics of local degradation in the alloy matrix is governed by the electrochemical reactivity of IMPs which changes during dealloying attack. On the other hand, it seems that the galvanic interactions take place quite locally and at the nanoscale between active zones of a corroding IMP and the closest alloy matrix. This phenomenon is directly attributed to the presence of the isolating corrosion products, in particular aluminium (hydr)oxide, that cannot support electrochemical reactions and physically cover electrochemically active locations [16]. Here, dedicated nanoscopic morphological and compositional observations imply that the early stages of local corrosion in AAs are more complicated than the relatively simple microgalvanic interactions between cathodic IMPs and their surrounding alloy matrix considered to date [31,32,34]. Dealloying attack is indeed the precursor of corrosion initiation whilst intrinsic electrochemical instability is a parameter that greatly drive the kinetics of local degradation. This is particularly noticeable for composite $Al_7Cu_2Fe$(Mn)/$Al_{76}Cu_6Fe_7Mn_5Si_6$ IMPs in which $Al_7Cu_2Fe$(Mn) domain undergoes dealloying far down from the surface while it is just a surface etching for $Al_{76}Cu_6Fe_7Mn_5Si_6$. In addition, discontinuous trenching merely close to the dealloyed parts of IMPs indicate the highly localized corrosion through nanogalvanic interactions. In fact, as long as the alloy matrix is covered with the isolating aluminium (hydr) oxide layer, it would be well protected. However, the local solution chemistry induced by dealloying of the corroding IMPs can weaken it, leading to local breakdown of the passive layer near the dealloyed region. The faster the dealloying through the intrinsic electrochemical instability of the IMPs happens, the earlier the adjacent alloy matrix dissolution takes place.

## 4. Overall local corrosion mechanism by intermetallic constituent phases and dispersoids

Our current findings in relation to early stage surface corrosion initiation through to moderate depth propagation allow us to propose a more detailed mechanism explaining local degradation events linked to nano- and microscopic intermetallic compounds. In fact, the local corrosion can be broken down into several stages including dealloying-driven initiation, trench initiation, depth propagation and particle undercutting as depicted schematically in Fig. 10. Besides, the type and location of electrochemical reactions taking place at and around cathodic intermetallic compounds are proposed in further detail.

### 4.1. Dealloying-driven initiation

Local corrosion initiates in the form of nano-pitting as a consequence of dealloying of IMPs which are electrochemically unstable in aqueous electrolytes and undergo preferential dissolution of their active elemental constituents [29]. At this stage, aluminium and manganese

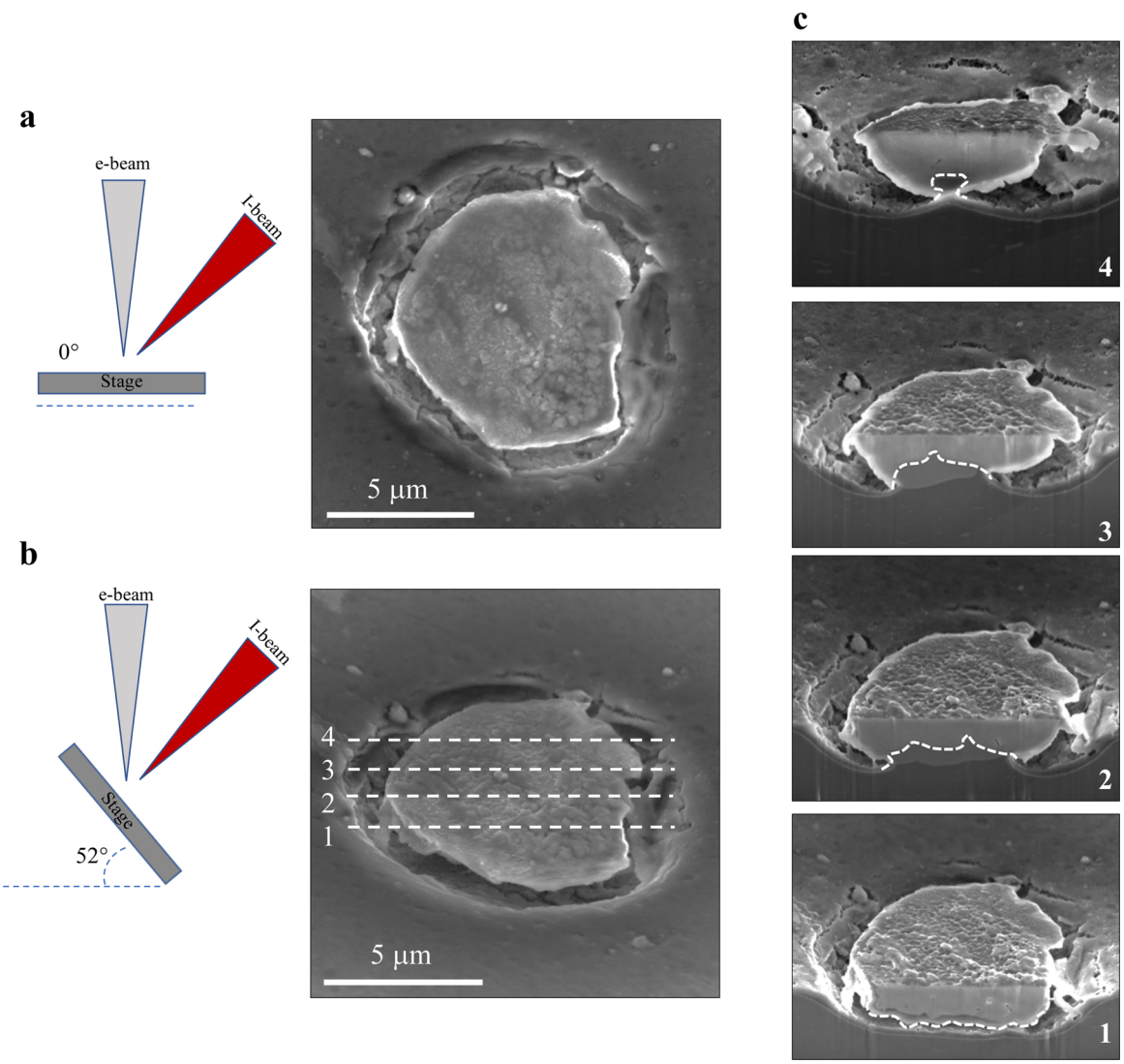


**Fig. 6.** FIB/SEM analysis of local corrosion induced by $Al_7Cu_2Fe(Mn)$ phase. (a) Top-view SEM image of an $Al_7Cu_2Fe(Mn)$ particle immersed in 0.01 M NaCl for 19 h. (b) SEM image of the same IMP when the stage is tilted at 52 °. (c) SEM images of the FIB serial sections along the lines shown in Fig. 6b. The white dashed curves separate the dealloyed region from the intact part of the particle.

largely, and iron slightly get corroded while the dissolution of copper is not thermodynamically favoured and gets redistributed through surface diffusion, leading to aggregated regions of copper and iron. The Cu- and Fe-rich regions can establish nano-galvanic coupling to drive anodic dissolution of the rest of the particle as they acquire a higher corrosion potential and can accommodate ORR efficiently. The enhanced nobility causes a greater driving force for local breakdown within the adjacent alloy matrix which is covered by an aluminium (hydr)oxide passive layer. Note that the aluminium (hydr)oxide is isolating in nature and cannot support electrochemical reactions [17].

### 4.2. Trench initiation

With prolonged exposure time, the local dissolution rates in the particle and alloy matrix increase. This phenomenon gradually leads to an enhanced alkaline local chemistry in which the passive layer gets undermined [11] and subsequently the underlying metal would undergo uniform dissolution. Therefore, local corrosion occurs by discontinuous trenching within the alloy matrix at the matrix/particle interface closest to the dealloyed region. The electrochemical instability of intermetallic compounds largely governs the kinetics of degradation at this stage. As a token of this root cause of kinetic variations across different IMPs, the difference between $Al_7Cu_2Fe(Mn)$ and $Al_{76}Cu_6Fe_7Mn_5Si_6$ is typical at this stage; dealloying penetrates rather fast into $Al_7Cu_2Fe(Mn)$ phase as a consequence of selective dissolution of manganese and aluminium, and iron to a minor extent. To preserve the charge balance, the top part of the corroding particle has to accommodate the cathodic reactions at a high rate that produces a highly basic local chemistry in which the nearest alloy matrix starts to locally dissolve.

### 4.3. Depth propagation

Given the importance of IMP chemical composition, progressive dealloying controls the electrochemical reactivity of IMPs as Cu- and Fe-rich locations on a corroding IMP are highly noble that can actively support cathodic reactions and drive anodic dissolution of the adjacent alloy matrix. In contrast, silicon can largely hinder the electrochemical reactivity since during its oxidation, it turns into $SiO_2$ which is semiconducting but stable in a wide range of pH [57]. Manganese is highly soluble in neutral and acidic solutions and hence etched away at the beginning of exposure [57]. Aluminium is electrochemically active in nature; however, its (hydr)oxide form is stable at pH 4-9 [57]. At early stages of corrosion, the corroded region can be passivated by the

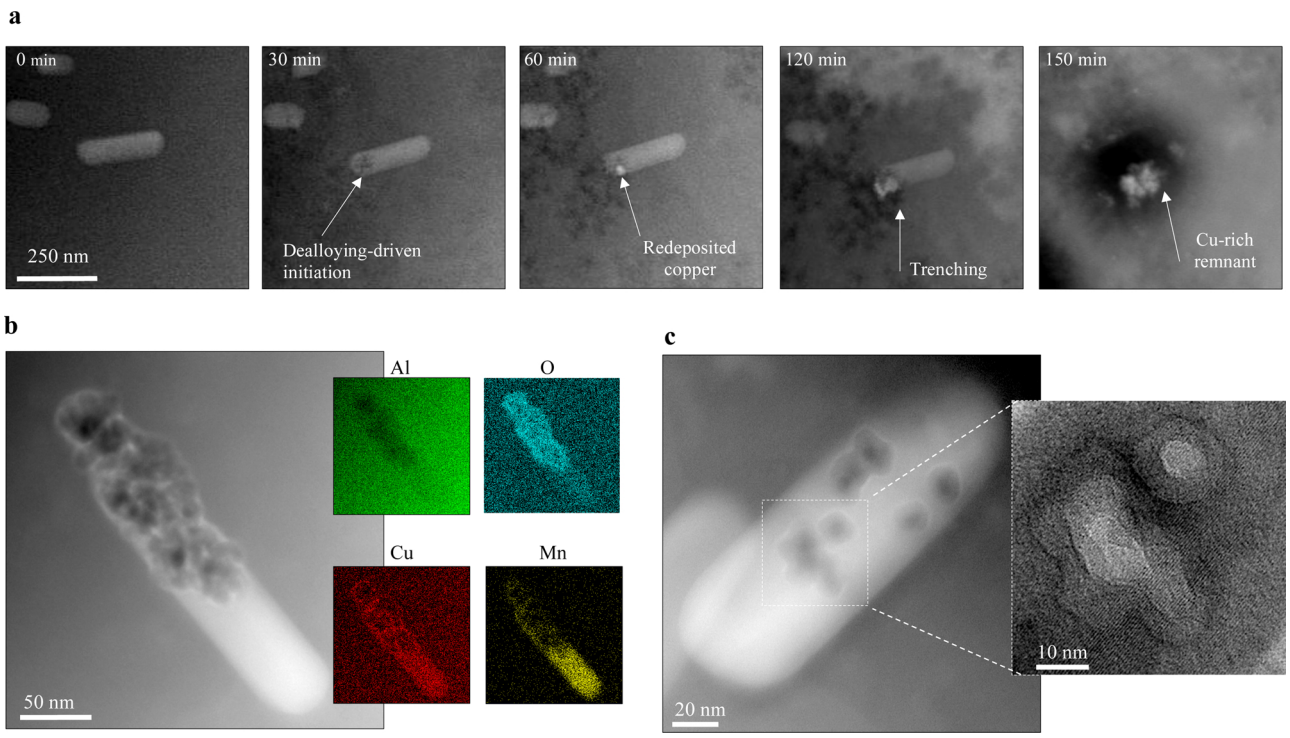


**Fig. 7.** Local corrosion induced by nanoscopic dispersoid $Al_{20}Mn_3Cu_2$. (a) HAADF-STEM images of an a dispersoid particle at different stages of corrosion. (b) STEM/EDS analysis a locally-dissolved dispersoid particle after a 20-min exposure to distilled water. (c) HAADF-STEM image of a dispersoid particle exposed to distilled water for 20 min, revealing dealloying at the particle itself. The inset is high resolution TEM image taken from the rectangular region.

formation of an aluminium (hydr)oxide layer (see Fig. 1a at 120 min). However, it cannot withstand the established galvanic interaction and the consequent aggressive local solution chemistry, hence would chemically dissolve (Fig. 1a). In fact, the presence of aluminium (hydr) oxide, which is isolating, can physically cover the electrochemically active sites and leads to galvanic interactions within nanometric distances only, in particular at very early stages of corrosion. Note that Cu may also undergo oxidation inside the corroding IMPs, turning into $Cu_2O$ during the depth propagation step of local corrosion. This phenomenon can occur as a consequence of physical or electrical isolation

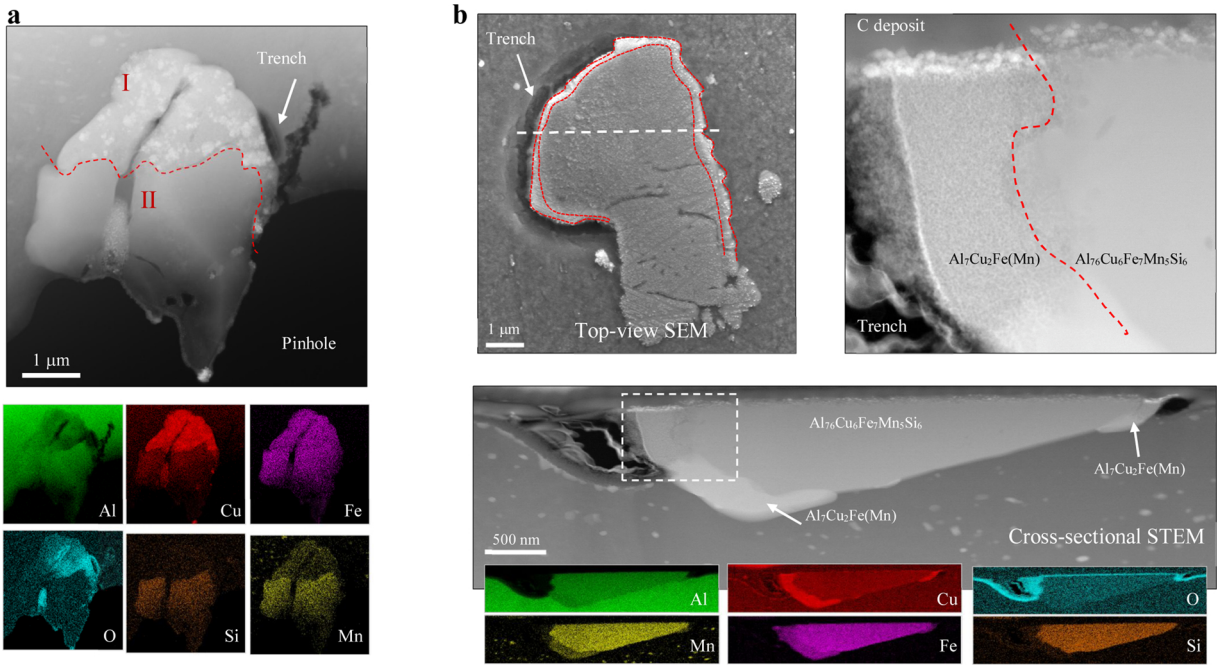


**Fig. 8.** Local corrosion induced by composite $Al_7Cu_2Fe(Mn)/Al_{76}Cu_6Fe_7Mn_5Si_6$ particles. (a) Top-view STEM/EDS analysis of a composite particle on an argon ion-milled specimen exposed to 0.01 M NaCl for 320 min. Region I is identified as $Al_7Cu_2Fe(Mn)$ which is distinguished by the red dashed line from $Al_7Cu_6Fe_7Mn_5Si_6$ domain (Region II). (b) Top-view SEM and cross-sectional STEM/EDS analysis of a composite particle on a bulk sample immersed in 0.01 M NaCl for 6 h. The cross-section is lifted out along the white dashed line. The inset shows the zoomed-in STEM image of the white rectangular region, indicating the deep penetration of dealloying into the $Al_7Cu_2Fe(Mn)$ domain.

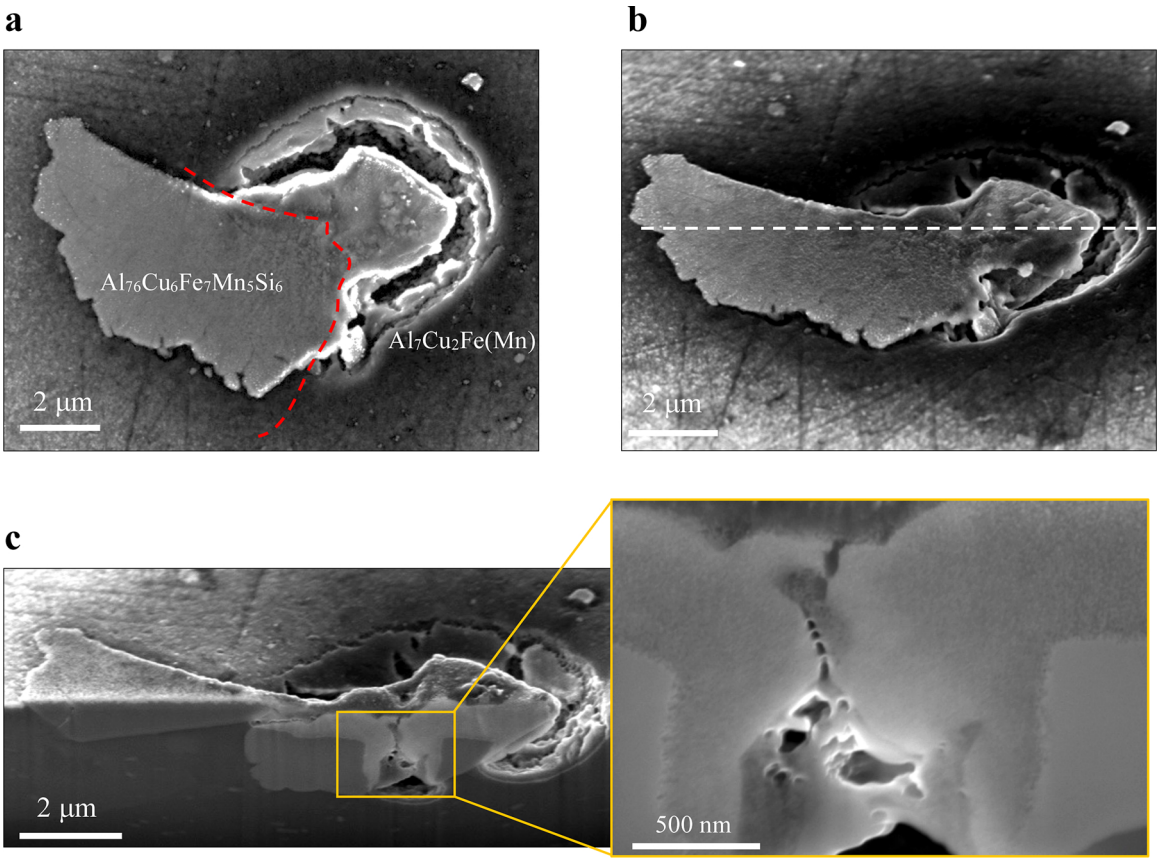


**Fig. 9.** FIB/SEM analysis of local corrosion induced by a composite $Al_7Cu_2Fe(Mn)/Al_{76}Cu_6Fe_7Mn_5Si_6$ particle. (a) Top-view SEM image of a composite $Al_7Cu_2Fe(Mn)/Al_{76}Cu_6Fe_7Mn_5Si_6$ particle immersed in 0.01 M NaCl for 19 h. (b) SEM image of the same composite IMP when the stage is tilted at 52 °. (c) Cross-sectional SEM image along the dashed line shown in Fig. 9b. The inset is a closer look at the orange rectangular region, revealing a deep penetration of dealloying into the $Al_7Cu_2Fe(Mn)$ domain where the alloy matrix is trenched far down from the surface.

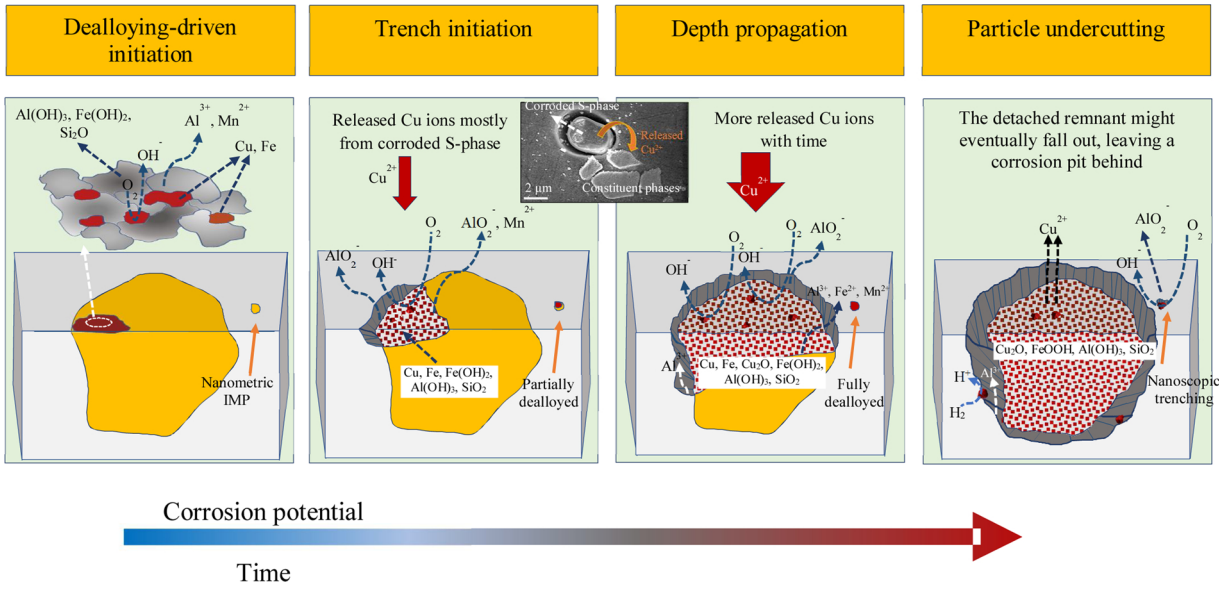


**Fig. 10.** Dealloying-driven local corrosion mechanism. 3D schematic view of localized corrosion initiation induced by cathodic dispersoids and constituent phases. The probable corrosion reactions occurring around IMPs are depicted in detail. As schematically shown, corrosion initiates at the surface of the particle itself and then simultaneously propagates in the depth and trenches the closest alloy matrix through nanogalvanic interactions. The inset is a top-view SEM image taken from a post-corroded sample, showing released copper from a dealloyed $Al_2CuMg$ (S-phase) and redeposited on other IMPs and the alloy matrix around.

of some copper segments [58]. All the constituent compounds are of higher electrochemical stability than active phase like $Al_2CuMg$ [29,58]. Thus, local degradation induced by the latter takes place over a relatively shorter time-scale; associated with the release of copper ions that can get redeposited on the top of nearby corroding constituent IMPs [28,59–64], as the SEM inset shows in Fig. 10. Besides, in a work using liquid-phase TEM, we have evidenced that corroded S-phase particles largely release copper ions to the solution upon the particle undercutting process which can be redeposited on the active sites of the alloy surface like other corroding IMPs [58]. This phenomenon can greatly contribute to the enhanced cathodic activity of the IMPs, leading to nano-galvanic coupling within the corroding IMPs and with the closest alloy matrix. Thus, the local dissolution of the matrix gradually trenches all around the particle and corrosion simultaneously propagates into the matrix and corroding IMP. The more reactive the corroding intermetallic compound is, the deeper corrosion propagates into it.

### 4.4. Particle undercutting

The local dissolution continues to dissolve the alloy matrix until undercutting the particle. At this point, the corroding IMPs can acquire higher corrosion potentials and end up as a fully dealloyed remnant. Afterwards, some copper can be released from the particle as the corrosion potential of the undercut IMP would be high enough for copper dissolution [29]. The remnant might later fall out and leave behind a corrosion pit. The whole mechanism is the same for sub-micron dispersoids, albeit occurring over a shorter time- and smaller length-scales shown in Fig. 10 as well.

## 5. Conclusions

Time-resolved top-view nanoscopic observations along with complementary cross-sectional post-mortem investigations confirm that cathodic phases evolve microstructurally and compositionally during local corrosion. Local corrosion basically initiates at cathodic intermetallic compounds in the form of dealloying attack (mainly selective dissolution of Al and Mn) as they are electrochemically unstable themselves. Trenching initiates closest to the dealloyed region as a consequence of the local solution chemistry being established initially due to nanogalvanic interactions within a corroding IMP. Besides, the galvanic interactions between dealloyed regions of IMPs and the adjacent alloy matrix stabilise local degradations. The intrinsic electrochemical stability of intermetallic compounds is proposed as the main controlling factor driving the kinetics of local degradation rather than the numerously reported corrosion potential (surface Volta potential) difference between the cathodic particle and the surrounding matrix. This is based on direct nanoscopic observations of composite $Al_7Cu_2Fe$ (Mn)/$Al_{76}Cu_6Fe_7Mn_5Si_6$ IMPs where the noble domain ($Al_7Cu_2Fe$(Mn)) shows dealloying far down from the surface, causing deep discontinuous trenching of the alloy matrix in the closest vicinity at a faster rate than that adjacent to the adjacent $Al_{76}Cu_6Fe_7Mn_5Si_6$ domain. Although the presence of noble elements like Cu and Fe greatly contributes to electrochemical reactivity of intermetallic compounds, it is largely hindered by other elements like Al and Si due to the formation of isolating or semi-conductive corrosion products that are unable of supporting electrochemical reactions. Besides, the redeposited copper sourced from corroding particles, such as $Al_2CuMg$, can accelerate the kinetics of the IMPs dealloying and local alloy matrix degradation. The nanoscopic dispersoids $Al_{20}Mn_3Cu_2$ undergo similar degradation stages but over a shorter time- and length-scale.

## Data and materials availability

All the data needed to assess the conclusions in the work is presented in the paper and/or the Supplementary Materials.

## CRediT authorship contribution statement

**A. Kosari:** Conceptualization, Methodology, Validation, Investigation, Writing - original draft. **F. Tichelaar:** Conceptualization, Writing - review & editing. **P. Visser:** Conceptualization, Writing - review & editing. **H. Zandbergen:** Conceptualization, Writing - review & editing, Supervision. **H. Terryn:** Conceptualization, Writing - review & editing, Supervision. **J.M.C. Mol:** Conceptualization, Writing - review & editing, Supervision.

## Declaration of Competing Interest

The authors declare that they have no Conflict of interest.

## Acknowledgement

This work is part of the research programme Understanding Processes using Operando Nanoscopy (UPON) with project number 14205 (B2), which is financed by Nederlandse Organisatie voor Wetenschappelijk Onderzoek (NWO) and partly by AkzoNobel.

## Appendix A. Supplementary data

Supplementary material related to this article can be found, in the online version, at doi:https://doi.org/10.1016/j.corsci.2020.108947.

## References

[1] P. Rambabu, N. Eswara Prasad, V.V. Kutumbarao, R.J.H. Wanhill, Aluminium Alloys for Aerospace Applications, in: N.E. Prasad, R.J.H. Wanhill (Eds.), Aerospace Materials and Material Technologies, Volume 1 Aerospace Materials, Springer Singapore, Singapore, 2017, pp. 29–52.
[2] G. Frankel, WR Whitney Award Lecture: The Effects of Microstructure and Composition on Al Alloy Corrosion, Corrosion 71 (2015) (2015) 1308–1320.
[3] A. Boag, A. Hughes, N. Wilson, A. Torpy, C. MacRae, A. Glenn, T. Muster, How complex is the microstructure of AA2024-T3? Corrosion Science 51 (2009) 1565–1568.
[4] J. Scully, D. Peebles, A. Romig, D. Frear, C. Hills, Metallurgical factors influencing the corrosion of aluminum, Al-Cu, and Al-Si alloy thin films in dilute hydrofluoric solution, Metallurgical Transactions A 23 (1992) 2641–2655.
[5] A.E. Hughes, R. Parvizi, M. Forsyth, Microstructure and corrosion of AA2024, Corrosion Reviews 33 (2015) 1–30.
[6] Z. Wang, P. Chen, H. Li, B. Fang, R. Song, Z. Zheng, The intergranular corrosion susceptibility of 2024 Al alloy during re–ageing after solution treating and cold–rolling, Corrosion Science 114 (2017) 156–168.
[7] M.-L. de Bonfils-Lahovary, L. Laffont, C. Blanc, Characterization of intergranular corrosion defects in a 2024 T351 aluminium alloy, Corrosion Science 119 (2017) 60–67.
[8] M.O. Speidel, Stress corrosion cracking of aluminum alloys, Metallurgical Transactions A 6 (1975) 631.
[9] A. Boag, A. Hughes, A. Glenn, T. Muster, D. McCulloch, Corrosion of AA2024-T3 Part I: Localised corrosion of isolated IM particles, Corrosion Science 53 (2011) 17–26.
[10] J. De Wit, Local potential measurements with the SKPFM on aluminium alloys, Electrochimica Acta 49 (2004) 2841–2850.
[11] A.E. Hughes, N. Birbilis, J.M. Mol, S.J. Garcia, X. Zhou, G.E. Thompson, High strength Al-alloys: microstructure, corrosion and principles of protection, Recent Trends in Processing and Degradation of Aluminium Alloys 1 (2011).
[12] A. Boag, R. Taylor, T. Muster, N. Goodman, D. McCulloch, C. Ryan, B. Rout, D. Jamieson, A. Hughes, Stable pit formation on AA2024-T3 in a NaCl environment, Corrosion Science 52 (2010) 90–103.
[13] G. Ilevbare, O. Schneider, R. Kelly, J. Scully, In situ confocal laser scanning microscopy of AA 2024-T3 corrosion metrology I. Localized corrosion of particles, Journal of The Electrochemical Society 151 (2004) B453–B464.
[14] J. Li, J. Dang, A summary of corrosion properties of Al-rich solid solution and secondary phase particles in Al alloys, Metals 7 (2017) 84.
[15] R. Parvizi, M.Y. Tan, A.E. Hughes, Recent Insights into Corrosion Initiation at the Nanoscale, Fundamentals of Aluminium Metallurgy, Elsevier, 2018, pp. 525–551.
[16] N. Wint, Z. Barrett, G. Williams, H. McMurray, The Study of AA2024 De-Alloying Using Luminol Electrogenerated Chemiluminescence Imaging, Journal of The Electrochemical Society 166 (2019) C3417–C3430.
[17] Z. Szklarska-Smialowska, Pitting corrosion of aluminum, Corrosion science 41 (1999) 1743–1767.
[18] C. Liu, S.K. Malladi, Q. Xu, J. Chen, F.D. Tichelaar, X. Zhuge, H.W. Zandbergen, In-situ STEM imaging of growth and phase change of individual CuAl X precipitates in Al alloy, Scientific reports 7 (2017) 1–8.
[19] S.K. Malladi, Q. Xu, M.A. van Huis, F.D. Tichelaar, K.J. Batenburg, E. Yücelen,

B. Dubiel, A. Czyrska-Filemonowicz, H.W. Zandbergen, Real-time atomic scale imaging of nanostructural evolution in aluminum alloys, Nano letters 14 (2014) 384–389.
[20] A.E. Hughes, A. Glenn, N. Wilson, A. Moffatt, A.J. Morton, R.G. Buchheit, A consistent description of intermetallic particle composition: An analysis of ten batches of AA2024-T3, Surface and interface analysis 45 (2013) 1558–1563.
[21] R.P. Wei, C.-M. Liao, M. Gao, A transmission electron microscopy study of constituent-particle-induced corrosion in 7075-T6 and 2024-T3 aluminum alloys, Metallurgical and Materials Transactions A 29 (1998) 1153–1160.
[22] N. Birbilis, Y. Zhu, S. Kairy, M. Glenn, J.-F. Nie, A. Morton, Y. Gonzalez-Garcia, H. Terryn, J. Mol, A. Hughes, A closer look at constituent induced localised corrosion in Al-Cu-Mg alloys, Corrosion Science 113 (2016) 160–171.
[23] L. Del Castillo, E. Lavernia, Microstructure and mechanical behavior of spray-deposited Al-Cu-Mg (-Ag-Mn) alloys, Metallurgical and materials transactions A 31 (2000) 2287–2298.
[24] A. Hughes, A. Boag, A. Glenn, D. McCulloch, T. Muster, C. Ryan, C. Luo, X. Zhou, G. Thompson, Corrosion of AA2024-T3 Part II: Co-operative corrosion, Corrosion Science 53 (2011) 27–39.
[25] N. Birbilis, T.H. Muster, R.G. Buchheit, Corrosion of Aluminum Alloys, in: P. Marcus (Ed.), Corrosion mechanisms in theory and practice, CRC press, 2011.
[26] V. Guillaumin, P. Schmutz, G. Frankel, Characterization of corrosion interfaces by the scanning Kelvin probe force microscopy technique, Journal of the Electrochemical Society 148 (2001) B163–B173.
[27] P. Schmutz, G. Frankel, Characterization of AA2024-T3 by scanning Kelvin probe force microscopy, Journal of the Electrochemical Society 145 (1998) 2285–2295.
[28] L. Lacroix, L. Ressier, C. Blanc, G. Mankowski, Combination of AFM, SKPFM, and SIMS to study the corrosion behavior of S-phase particles in AA2024-T351, Journal of the Electrochemical Society 155 (2008) C131–C137.
[29] S. Lebouil, J. Tardelli, E. Rocca, P. Volovitch, K. Ogle, Dealloying of $Al_2Cu$, $Al_7Cu_2Fe$, and $Al_2CuMg$ intermetallic phases to form nanoparticulate copper films, Materials and Corrosion 65 (2014) 416–424.
[30] R. Buchheit, A compilation of corrosion potentials reported for intermetallic phases in aluminum alloys, Journal of the Electrochemical Society 142 (1995) 3994.
[31] N. Birbilis, R. Buchheit, Investigation and discussion of characteristics for intermetallic phases common to aluminum alloys as a function of solution pH, Journal of The Electrochemical Society 155 (2008) C117–C126.
[32] N. Birbilis, R.G. Buchheit, Electrochemical characteristics of intermetallic phases in aluminum alloys an experimental survey and discussion, Journal of The Electrochemical Society 152 (2005) B140–B151.
[33] K.D. Ralston, T.L. Young, R.G. Buchheit, Electrochemical evaluation of constituent intermetallics in aluminum alloy 2024-T3 exposed to aqueous vanadate inhibitors, Journal of the electrochemical society 156 (2009) C135–C146.
[34] N. Birbilis, M.K. Cavanaugh, R.G. Buchheit, Electrochemical behavior and localized corrosion associated with $Al_7Cu_2Fe$ particles in aluminum alloy 7075-T651, Corrosion Science 48 (2006) 4202–4215.
[35] B. Mazurkiewicz, A. Piotrowski, The electrochemical behaviour of the $Al_2Cu$ intermetallic compound, Corrosion Science 23 (1983) 697–707.
[36] L. Yin, Y. Jin, C. Leygraf, N. Birbilis, J. Pan, Numerical Simulation of Micro-Galvanic Corrosion in Al Alloys: Effect of Geometric Factors, Journal of the Electrochemical Society 164 (2017) C75–C84.
[37] O. Schneider, G. Ilevbare, J. Scully, R. Kelly, In situ confocal laser scanning microscopy of AA 2024-T3 corrosion metrology II. Trench formation around particles, Journal of The Electrochemical Society 151 (2004) B465–B472.
[38] J. Wloka, S. Virtanen, Detection of nanoscale $\eta$-$MgZn_2$ phase dissolution from an Al-Zn-Mg-Cu alloy by electrochemical microtransients, Surface and Interface Analysis: An International Journal devoted to the development and application of techniques for the analysis of surfaces, interfaces and thin films 40 (2008) 1219–1225.
[39] A. Laurino, E. Andrieu, J.-P. Harouard, J. Lacaze, M.-C. Lafont, G. Odemer, C. Blanc, Corrosion behavior of 6101 aluminum alloy strands for automotive wires, Journal of The Electrochemical Society 160 (2013) C569–C575.
[40] S.K. Kairy, N. Birbilis, Clarifying the Role of $Mg_2Si$ and Si in Localized Corrosion of Aluminum Alloys by Quasi In Situ Transmission Electron Microscopy, Corrosion 76 (2020) 464–475.
[41] B. Zhang, J. Wang, B. Wu, E. Oguzie, K. Luo, X. Ma, Direct observation of atomic-scale origins of local dissolution in Al-Cu-Mg alloys, Scientific reports 6 (2016) 39525.
[42] J. Wang, B. Zhang, Y. Zhou, X. Ma, Multiple twins of a decagonal approximant embedded in S-Al2CuMg phase resulting in pitting initiation of a 2024Al alloy, Acta Materialia 82 (2015) 22–31.
[43] X. Zhang, T. Hashimoto, J. Lindsay, X. Zhou, Investigation of the de-alloying behaviour of θ-phase ($Al_2Cu$) in AA2024-T351 aluminium alloy, Corrosion Science 108 (2016) 85–93.
[44] Y. Zhu, K. Sun, J. Garves, L.G. Bland, J. Locke, J. Allison, G. Frankel, Micro-and nano-scale intermetallic phases in AA2070-T8 and their corrosion behavior, Electrochimica Acta 319 (2019) 634–648.
[45] Y. Zhu, G. Frankel, Effect of major intermetallic particles on localized corrosion of AA2060-T8, Corrosion 75 (2019) 29–41.
[46] Y. Zhu, K. Sun, G. Frankel, Intermetallic phases in aluminum alloys and their roles in localized corrosion, Journal of The Electrochemical Society 165 (2018) C807–C820.
[47] C. Örnek, C. Leygraf, J. Pan, Real-Time Corrosion Monitoring of Aluminum Alloy Using Scanning Kelvin Probe Force Microscopy, Journal of The Electrochemical Society 167 (2020) 081502.
[48] L. Yin, Y. Jin, C. Leygraf, J. Pan, A FEM model for investigation of micro-galvanic corrosion of Al alloys and effects of deposition of corrosion products, Electrochimica Acta 192 (2016) 310–318.
[49] S. Malladi, F. Tichelaar, Q. Xu, M. Wu, H. Terryn, J. Mol, F. Hannour, H. Zandbergen, Quasi in situ analytical TEM to investigate electrochemically induced microstructural changes in alloys: AA2024-T3 as an example, Corrosion science 69 (2013) 221–225.
[50] B. Zhang, J. Wang, B. Wu, Y. Zhou, X. Ma, Quasi-in-situ ex-polarized TEM observation on dissolution of MnS inclusions and metastable pitting of austenitic stainless steel, Corrosion Science 100 (2015) 295–305.
[51] Y. Zhang, P. Gore, W. Rong, Y. Wu, Y. Yan, R. Zhang, L. Peng, J.-F. Nie, N. Birbilis, Quasi-in-situ STEM-EDS insight into the role of Ag in the corrosion behaviour of Mg-Gd-Zr alloys, Corrosion Science 136 (2018) 106–118.
[52] Y. Zhu, J.D. Poplawsky, S. Li, R.R. Unocic, L.G. Bland, C.D. Taylor, J.S.W. Locke, E.A. Marquis, G.S. Frankel, Localized corrosion at nm-scale hardening precipitates in Al-Cu-Li alloys, Acta Materialia (2020) 204–213.
[53] A. Kosari, H. Zandbergen, F. Tichelaar, P. Visser, H. Terryn, A. Mol, Application of In Situ Liquid Cell Transmission Electron Microscopy in Corrosion Studies: A Critical Review of Challenges and Achievements, Corrosion 76 (2020) 4–17.
[54] D.B. Williams, C.B. Carter, The transmission electron microscope, Transmission electron microscopy, Springer, 1996, pp. 3–17.
[55] J. Mayer, L.A. Giannuzzi, T. Kamino, J. Michael, TEM sample preparation and FIB-induced damage, MRS bulletin 32 (2007) 400–407.
[56] J. Erlebacher, M.J. Aziz, A. Karma, N. Dimitrov, K. Sieradzki, Evolution of nanoporosity in dealloying, Nature 410 (2001) 450–453.
[57] M. Pourbaix, Atlas of Electrochemical Equilibria in Aqueous Solutions, National Association of Corrosion Engineers, Houston, TX, 1974, pp. 384–392 2nd English edn.
[58] A. Kosari, H. Zandbergen, F. Tichelaar, P. Visser, P. Taheri, H. Terryn, J.M.C. Mol, In-situ nanoscopic observations of dealloying-driven local corrosion from surface initiation to in-depth propagation, Corrosion Science (2020) 108912.
[59] R. Buchheit, M. Martinez, L. Montes, Evidence for Cu ion formation by dissolution and dealloying the $Al_2CuMg$ intermetallic compound in rotating ring-disk collection experiments, Journal of The Electrochemical Society 147 (2000) 119–124.
[60] N. Dimitrov, J. Mann, K. Sieradzki, Copper redistribution during corrosion of aluminum alloys, Journal of the Electrochemical Society 146 (1999) 98.
[61] M. Vukmirovic, N. Dimitrov, K. Sieradzki, Dealloying and corrosion of Al alloy 2024 T 3, Journal of The Electrochemical Society 149 (2002) B428–B439.
[62] T. Hashimoto, X. Zhang, X. Zhou, P. Skeldon, S. Haigh, G. Thompson, Investigation of dealloying of S phase ($Al_2CuMg$) in AA 2024-T3 aluminium alloy using high resolution 2D and 3D electron imaging, Corrosion Science 103 (2016) 157–164.
[63] R. Buchheit, R. Grant, P. Hlava, B. McKenzie, G. Zender, Local dissolution phenomena associated with S phase ($Al_2CuMg$) particles in aluminum alloy 2024-T3, Journal of the electrochemical society 144 (1997) 2621.
[64] L. Lacroix, L. Ressier, C. Blanc, G. Mankowski, Statistical study of the corrosion behavior of $Al_2CuMg$ intermetallics in AA2024-T351 by SKPFM, Journal of the Electrochemical Society 155 (2008) C8–C15.